Lagrangian statistics in compressible turbulence: Evolution of deformation gradient tensor and flow-field topology

Nishant Parashar[1]†, Sawan Suman Sinha [1] and Balaji Srinivasan[2]

[1]Department of Applied Mechanics, Indian Institute of Technology Delhi, New Delhi 110016, India

[2]Department of Mechanical Engineering, Indian Institute of Technology Madras, Chennai 600036, India

(Received xx; revised xx; accepted xx)

1. Introduction

The gradients of the small-scale velocity field and its dynamics in a turbulent flow hold the key to understanding many important nonlinear turbulence processes like cascade, mixing, intermittency and material element deformation. Thus, examination of the velocity gradient tensor in several canonical turbulent flow fields have been pursued using experimental measurements (Lüthi *et al.* (2005)), direct numerical simulations (DNS, Ashurst *et al.* (1987)), and even by employing simpler autonomous dynamical models (ordinary differential equations, Vieillefosse (1982); Cantwell (1992)) of velocity gradients. The pioneering work done by these authors have been further followed up extensively by several researchers for both incompressible (Girimaji (1991); Girimaji & Speziale (1995); Ohkitani (1993); Pumir (1994); O'Neill & Soria (2005); Chevillard & Meneveau (2006, 2011)) and compressible turbulence (Pirozzoli & Grasso (2004); Suman & Girimaji (2009, 2010*b*, 2012); Danish *et al.* (2016*a*); Parashar *et al.* (2017*a*)). These efforts have led to an improved understanding of small-scale turbulence.

Most DNS or experiment-based studies of fluid mechanics have so far been performed using one-time Eulerian flow field. It is desirable to investigate the statistics following individual fluid particles (the Lagrangian tracking). Such an investigation is especially required from the point of view of developing/improving simple models like the restricted Euler equation (REE) (Cantwell (1992); Girimaji & Speziale (1995); Meneveau (2011)) for incompressible flows and the enhanced homogenized Euler equation model of Suman & Girimaji (2009) for compressible flows. Such simple models, in turn, can be used for closure of Lagrangian PDF method of turbulence (Pope (2002)). An apt example of how Lagrangian statistics can reveal deeper insights into velocity gradient dynamics is the recent experimental study of Xu *et al.* (2011), wherein the authors provided evidence of the so-called "Pirouette effect". Even though the vorticity vector has always been expected to align with the largest strain-rate eigenvector, Eulerian investigations invariably reveal a counterintuitive picture of vorticity aligning most strongly with the intermediate eigenvector of the instantaneous local strain-rate tensor. Xu *et al.* (2011), with their experimental Lagrangian investigations, provided first-hand evidence that indeed the vorticity vector dynamically attempts to align with the largest strain-rate eigenvector at an initial reference time in order to cause intense vortex stretching, and

† Email address for correspondence: nishantparashar14@gmail.com

the alignment tendency as shown by Eulerian one time field (with the instantaneous intermediate eigenvector) was merely a transient and incidental event.

In incompressible flows, Lagrangian studies using the direct numerical simulation of decaying turbulence have earlier been performed by Yeung & Pope (1989), though the authors' focus was on Lagrangian statistics of velocity, acceleration and dissipation. In compressible turbulence, Lagrangian statistics of velocity gradients have been recently studied by Danish *et al.* (2016*a*) and Parashar *et al.* (2017*a*). While Danish *et al.* (2016*a*) provided the first glimpse of compressibility effects on the alignment tendencies of the vorticity vector, Parashar *et al.* (2017*a*) followed it up and made attempts at explaining the observed behaviour in terms of the dynamics of the inertia tensor of fluid particles and conservation of angular momentum of tetrads representing the fluid particles (using the idea of Chertkov *et al.* (1999)). In continuation of our effort to develop deeper insight into the dynamics of small-scale turbulence from a Lagrangian perspective, in this work, we focus on another two important aspects of velocity gradient dynamics: (i) evolution of the deformation gradient tensor, (ii) dynamics of flow field topology in compressible turbulence.

Our primary motivation behind investigating the dynamics of the deformation gradient tensor is that this quantity has been used in modelling the viscous processes in both the linear Lagrangian deformation model (LLDM, Jeong & Girimaji (2003)) and the enhanced homogenized Euler equation model (EHEE, Suman & Girimaji (2009)). While the first model is the simple dynamical representation of velocity gradient dynamics in incompressible flows, the EHEE model is the counterpart for compressible flows. Even though the EHEE model employing the LLDM approach does capture various Mach number and Prandtl number effects, further improvements are desirable (Danish *et al.* (2014)). From this point of view, in the first part of this work, we subject the LLDM modelling approach to a direct scrutiny by comparing its evolution history against that of the exact process it represents−an examination that has not been previously attempted. Direct numerical simulation data of decaying compressible turbulence over a wide range of Mach number along with a well-validated Lagrangian particle tracker is employed for the purpose. Further, the influence of compressibility−parameterized in terms of Mach number, dilatation rate and topology is also investigated.

In the second part of this work, we examine the evolution of topology itself in compressible turbulence following the exact Lagrangian trajectories of the invariants of the velocity gradient tensors. The local topology of a compressible flow field depends on the local state of the velocity gradient tensor. Topology can also be visualized as the local streamline pattern as observed with respect to a reference frame which is translating with the centre of mass of a local fluid particle (Chong *et al.* (1990)). Topology actually depends on the nature of eigenvalues of the velocity gradient tensor, and can also be readily determined by knowing the three invariants of the velocity gradient tensor. Topology is not only be used for visualization of a flow field, it has been observed to reveal deeper insights into various nonlinear turbulence processes as well (Cantwell (1993); Soria *et al.* (1994)). Recently, Danish *et al.* (2016*b*) have also attempted developing models for scalar mixing using topology as conditioning parameter.

Traditionally, due to the prohibitive demand of computational resources, dynamics of topology have been studied employing an approximate surrogate method called the conditional mean trajectories (CMT) proposed by Martín *et al.* (1998). The authors merely employed one-time velocity gradient data of the entire flow field and computed bin-averaged rates-of-change of second and third invariants using the right-hand-side of evolution equations of the invariants. These bin-averaged rates of change conditioned upon their locations were subsequently used to plot trajectories in the Q-R space. The authors called these trajectories as conditional mean trajectories (CMT) and used them as a surrogate approach to study invariant dynamics. Several authors have employed the CMTs to investigate various aspects of dynamic of topology both for incompressible (Ooi *et al.* (1999); Meneveau (2011); Atkinson *et al.* (2012)) and compressible flows (Chu & Lu (2013); Bechlars & Sandberg (2017)). Indeed the work done by previous researchers employing the approximate approach of CMTs have improved our understanding of the distribution and dynamics of topology in compressible turbulence. Even though CMTs provide useful information about dynamics of invariants, CMTs are afterall an approximation and merely a surrogate approach in teh absence of adequate computational resources (Martín *et al.* (1998)). An investigation of the exact Lagrangian dynamics in compressible turbulence must be performed, if adequate computational resources are available. Indeed such an investigation of invariants using exact Lagrangian trajectories have been recently performed by Bhatnagar *et al.* (2016) for incompressible turbulence. Thus, we identify the following objectives for the second part of this work: (i) identifying and understanding the differences, if any, between CMT and the exact Lagrangian trajectory (ELT) in compressible turbulence, and (ii) employing the ELTs to investigate lifetime of topologies and their interconversion processes.

To address the identified objectives of both parts of this paper, we employ direct numerical simulations of decaying isotropic compressible turbulence and over a wide range of turbulent Mach number (0.5, 1.5) and a moderate range of Reynolds number (70, 350). The exact Lagrangian dynamics are obtained using an almost time continuous set of flow field along with spline-aided Lagrangian particle tracker (more details in §4).

This paper is organized into seven sections. In §2 we present the governing equations. In §3 we provide details of our direct numerical simulations and the Lagrangian particle tracker. In §4 we explain our study plan. In §5 we evaluate the LLDM model of Jeong & Girimaji (2003) in terms of its ability to mimic the exact viscous diffusion process. In §6 we study the dynamics of topology, compare CMT and ELT and quantify the life of various flow-topologies existing in compressible turbulence. Section 7 concludes the paper with a summary.

2. Governing Equations

The governing equations of compressible flow field of a perfect gas are the continuity, momentum, energy and state equations:

$$\frac{\partial \rho}{\partial t} + V_k \frac{\partial \rho}{\partial x_k} = - \rho \frac{\partial V_k}{\partial x_k}; \tag{2.1}$$

$$\frac{\partial V_i}{\partial t} + V_k \frac{\partial V_i}{\partial x_k} = - \frac{1}{\rho}\frac{\partial p}{\partial x_i} + \frac{1}{\rho}\frac{\partial \sigma_{ik}}{\partial x_k}, \tag{2.2}$$

$$\frac{\partial T}{\partial t} + V_k \frac{\partial T}{\partial x_k} = - T(n-1)\frac{\partial V_i}{\partial x_i} - \frac{n-1}{\rho R}\frac{\partial q_k}{\partial x_k} + \frac{n-1}{\rho R}\frac{\partial}{\partial x_j}\left(V_i \sigma_{ji}\right), \tag{2.3}$$

$$p = \rho R T, \tag{2.4}$$

where V_i, x_i, ρ, p, T, R, σ_{ik}, q_k, n denote velocity, position, density, pressure, temperature, gas constant, stress tensor, heat flux and ratio of specific heat values, respectively. The quantities σ_{ij} and q_k obey the following constitutive relationships:

$$\sigma_{ij} = \mu \left(\frac{\partial V_i}{\partial x_j} + \frac{\partial V_j}{\partial x_i}\right) + \delta_{ij}\lambda \frac{\partial V_k}{\partial x_k}; \tag{2.5}$$

$$q_k = -K\frac{\partial T}{\partial x_k}, \tag{2.6}$$

where δ_{ij} is the Kronecker delta, K represents the thermal conductivity, and μ and λ denote the first and second coefficients of viscosity respectively $(\lambda = -\frac{2\mu}{3})$.

The velocity gradient tensor is defined as:

$$A_{ij} \equiv \frac{\partial V_i}{\partial x_j}.$$

The evolution equation of A_{ij} can be obtained by taking the gradient of momentum equation 2.2, as

$$\frac{DA_{ij}}{Dt} = -A_{ik}A_{kj} - \underbrace{\frac{\partial}{\partial x_j}\left(\frac{1}{\rho}\frac{\partial p}{\partial x_i}\right)}_{\mathbb{P}_{ij}} + \underbrace{\frac{\partial}{\partial x_j}\left\{\frac{1}{\rho}\frac{\partial}{\partial x_k}\left[\mu\left(\frac{\partial V_i}{\partial x_k} + \frac{\partial V_k}{\partial x_i} - \frac{2}{3}\frac{\partial V_p}{\partial x_p}\delta_{ik}\right)\right]\right\}}_{\Upsilon_{ij}}, \tag{2.7}$$

where, the operator $\frac{D}{Dt}(\equiv \frac{\partial}{\partial t} + V_k\frac{\partial}{\partial x_k})$ stands for the substantial derivative, which represents the rate of change following a fluid particle. In equation 2.7, the first term on its right-hand side (RHS) represents the self-deformation process of velocity-gradients. The term $\mathbb{P}_{ij}$ is called the pressure Hessian tensor, whereas Υ_{ij} represents the action of viscosity on the evolution of the velocity gradient tensor.

3. Direct numerical simulations and particle tracking

In this work dynamics of invariants of the velocity gradient tensor (VGT) are studied using the direct numerical simulation (DNS) of decaying turbulent flows. Our simulations are performed using the gas kinetic method (GKM). The gas kinetic method (GKM) was originally developed by Xu *et al.* (1996) has been shown to be quite robust in terms of numerical stability and has the ability to capture shock without numerical oscillations for simulating compressible turbulence (Kerimo & Girimaji 2007; Liao *et al.* 2009; Kumar *et al.* 2013; Parashar *et al.* 2017*b*). Our computational domain is of size 2π with a uniform grid and periodic boundary conditions imposed on opposite sides of the domain.

The initial velocity field is generated at random with zero mean and having the following energy spectrum $E(\kappa)$:

$$E(\kappa) = A_0\kappa^4 \exp\left(-2\kappa^2/\kappa_0^2\right), \tag{3.1}$$

where κ is wavenumber. Values for spectrum constants A_0 and κ_0 are provided in Table 1 for various simulations employed in this work. The relevant Reynolds number for isotropic turbulence is the one based on Taylor micro-scale (Re_λ):

$$Re_\lambda = \sqrt{\frac{20}{3\epsilon\nu}}k, \tag{3.2}$$

where k, ϵ, and ν represent turbulent kinetic energy, its dissipation-rate, and kinematic viscosity. For compressible isotropic turbulence, the relevant Mach number is the turbulent Mach number (M_t):

$$M_t = \sqrt{\frac{2K}{nR\overline{T}}}, \tag{3.3}$$

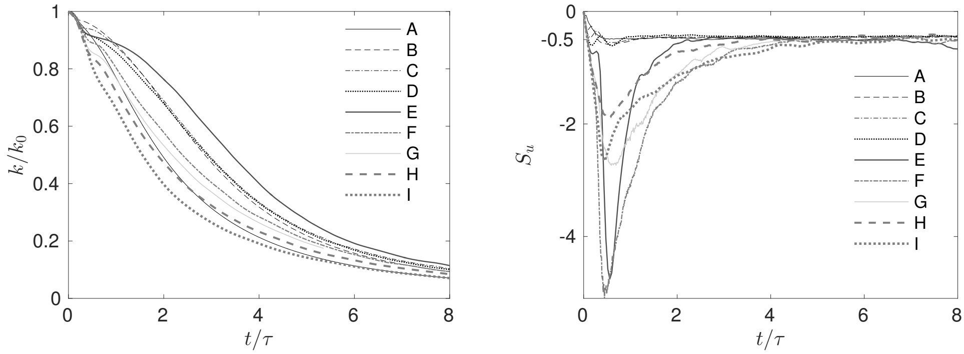

(a) (b)

FIGURE 1. Evolution of (a) normalized turbulent kinetic energy $\frac{k}{k_0}$ and (b) Velocity derivative skewness S_u, in Simulations A-I: (Table 1).

where $\overline{T}$ represents mean temperature. Following the work of Kumar *et al.* (2013), we have used 4^{th} order accurate weighted-essentially-non-oscillatory (WENO) method for interpolation of flow variables, in-order to simulate high Mach number compressible turbulent flows. Our solver has been extensively validated with established DNS results of compressible turbulent flows (Danish *et al.* (2016*a*)). In total, this study employs nine different simulations (Simulations A-I). Descriptions of these simulations are presented in Table 1.

In Figure 1(a) we present evolution of turbulent kinetic energy (K) observed in Simulations A-F. In Figure 1(b), we present the evolution of skewness of the velocity derivative (S_V) defined as:

$$k = \frac{1}{2}\overline{V_i V_i}; \tag{3.4}$$

$$S_{V_i} = \frac{\overline{\left(\frac{\partial V_i}{\partial x_i}\right)^3}}{\left[\overline{\left(\frac{\partial V_i}{\partial x_i}\right)^2}\right]^{3/2}}, \tag{3.5}$$

$$S_V = \frac{S_{V_1} + S_{V_2} + S_{V_3}}{3}. \tag{3.6}$$

Note that the time has been normalized using τ, which represents eddy turnover time (Yeung & Pope 1989; Elghobashi & Truesdell 1992; Samtaney *et al.* 2001; Martín *et al.* 2006).

$$\tau = \frac{\lambda_0}{u_0'}; \tag{3.7}$$

where u_0' and λ_0 are the root mean square (rms) velocity and integral-length-scale of the initial flow field (at time, $t = 0$). Since turbulence is considered realistic for velocity derivative skewness in the range of -0.6 to -0.4 (Lee *et al.* (1991)) over the Re_λ range employed in this work, we perform our study based on Lagrangian statistics for $t/\tau \geqslant 0.5$ while considering Simulations A-D and $t/\tau \geqslant 4.0$ for Simulations E-I (Figure 1(b)).

To extract Lagrangian statistics, a Lagrangian particle tracker (LPT) is used to extract the full time-history of tagged fluid particles. Our LPT obtains the trajectory $(\mathbf{X}^+(\mathbf{y}, \mathbf{t}))$

Simulation	Re_λ	M_t	Grid size	A_0	κ_0
A.	70	0.075	128^3	0.000023	4
B.	175	0.25	256^3	0.00026	4
C.	175	0.40	256^3	0.00066	4
D.	175	0.55	256^3	0.0013	4
E.	350	0.6	1024^3	0.0015	4
F.	150	1.0	512^3	0.0042	4
G.	100	1.0	512^3	0.0042	4
H.	70	1.0	256^3	0.0042	4
I.	70	1.5	256^3	0.0094	4

TABLE 1. Initial parameters of DNS simulations.

of a fluid particle by solving the following equation of motion:

$$\frac{\partial \mathbf{X}^{+}(t, \mathbf{y})}{\partial t} = \mathbf{V}\left(\mathbf{X}^{+}(t, \mathbf{y}), t\right), \tag{3.8}$$

where the superscript "+" represents a Lagrangian flow variable, and $\mathbf{y}$ indicates the label/identifier assigned to the fluid particle at a reference time (t_{ref}). The initial value of $\mathbf{X}^{+}$ at a reference time is chosen at random. Using this initial condition, we then integrate Equation 3.8 by employing second order Runge-Kutta method. However, upon integration, the position of the fluid particle at a subsequent time instant may not fall exactly on one of the grid points of computational domain used in the parent DNS. Therefore, an interpolation method is required to find relevant flow quantities at the particle's subsequent locations. Following the work of Yeung & Pope (1988), we choose cubic spline interpolation for this purpose. Like our DNS solvers, our LPT algorithm and implementation have been adequately validated. Details are available in Danish *et al.* (2016*a*).

4. Plan of study

In this section we present our plan of study and also explain the quantities that are employed to perform the desired investigations. In §4.1 we present the study plan for the first part of the work, which is the Lagrangian dynamics of the deformation gradient tensor. In §4.2 we explain our study plan for the second part of this work, which involves comparing CMT and ELT and consequently using these trajectories to investigate interconversion processes of topologies existing in compressible turbulence.

4.1. *Part I*

Equation 2.7 represents the exact evolution of the velocity gradient dynamics in compressible flows.

$$\Upsilon_{ij} = \underbrace{\nu \frac{\partial A_{ij}}{\partial x_k \partial x_k}}_{\Upsilon_I} + \underbrace{\nu \frac{\partial A_{kk}}{\partial x_i \partial x_j}}_{\Upsilon_{II}} - \underbrace{\frac{\nu}{\rho}\frac{\partial \rho}{\partial x_j}\left(\frac{\partial A_{ik}}{\partial x_k} + \frac{1}{3}\frac{\partial A_{kk}}{\partial x_i}\right)}_{\Upsilon_{III}} \tag{4.1}$$

In the first part of this work we focus on the viscous diffusion process (Υ_I). From the point of view of a dynamical equation of A_{ij} (like REE of) and HEE of)), the viscous diffusion term Υ_I represents a non-local, unclosed process. Jeong & Girimaji (2003) proposed a model for this process. This model is called the linear Lagrangian diffusion model (LLDM). The LLDM model approximates the viscous diffusion term Υ_I as:

$$\nu \frac{\partial A_{ij}}{\partial x_k \partial x_k} \approx \frac{C^{-1}_{kk}}{3\tau_\nu} A_{ij}, \tag{4.2}$$

where, $\mathbf{C}$ represents the right Cauchy Green tensor, which is derived from the deformation gradient tensor $\mathbf{D}$:

$$D_{ij} \equiv \frac{\partial x_i}{\partial X_j}. \tag{4.3}$$

$$C_{ij} \equiv D_{ki} D_{kj}. \tag{4.4}$$

Suman & Girimaji (2009) have employed the same LLDM model for the closure of their enhanced homogenized Euler equation model (EHEE). Even though the LLDM achieves a mathematically closed form, in this work we intend to perform a direct scrutiny of this model using our DNS results. Such an investigation is required for a deeper understanding of the model and may lead to further improvement in its performance.

Our interest is to examine how the viscous process Υ_I undergoes changes in comparison to its state at a reference time following a fluid particle. For monitoring this change we define an amplification ratio $r(t, t_{ref}$:

$$r(t, t_{ref}) = \frac{\sqrt{\Upsilon_{I_{ij}}(t)\Upsilon_{I_{ij}}(t)}}{\sqrt{\Upsilon_{I_{ij}}(t_{ref})\Upsilon_{I_{ij}}(t_{ref})}}, \tag{4.5}$$

where, $\Upsilon_{I_{ij}}(t)$ and $\Upsilon_{I_{ij}}(t_{ref})$ are values of the quantity $\Upsilon_{I_{ij}}$ associated with an identified fluid particle at time t and reference time t_{ref} respectively. Since an individual particle represents just one realization, we obtain a relevant statistics by calculating the mean of $r(t, t_{ref})$ over several identified fluid particles of a homogeneous flow field. The resulting quantity is referred as $\langle r(t, t_{ref})\rangle$, and is truly a two-time Lagrangian correlation. Direct numerical simulation of compressible decaying turbulence along with our Lagrangian particle tracker (LPT) are employed to access $\langle r(t, t_{ref})\rangle$. A set of 1,000,000 particles are identified at t_{ref} for the purpose. Further, to identify the role of turbulent Mach number (M_t), normalized dilatation (a_{ii}) and topology ($\mathcal{T}$), we also calculate $\langle r(t, tref)\rangle$ conditioned upon selected particles with a specified M_t, or a_{ii} or $\mathcal{T}$ at t_{ref}. These conditional statistics are denoted as $\langle r(t, t_{ref})|M_t\rangle$, $\langle r(t, t_{ref})|a_{ii}\rangle$ and $\langle r(t, t_{ref})|\mathcal{T}\rangle$ respectively.

Further, we compare the Lagrangian statistics of the LLDM model term against that of the exact viscous process Υ_I. In order to understand the flaws in the LLDM model (if any), we revisit the modelling assumptions by presenting the step-by-step derivation of the LLDM model term from Υ_I. Using Eulerian-Lagrangian change of variables, LLDM approach of Jeong & Girimaji (2003) models the viscous term (Υ_I) as follows:

$$\nu \frac{\partial^2 A_{ij}}{\partial x_k \partial x_k} = \nu \frac{\partial}{\partial x_k} \left(\frac{\partial X_n}{\partial x_k} \frac{\partial A_{ij}}{\partial X_n} \right) \tag{4.6}$$

$$\nu \frac{\partial^2 A_{ij}}{\partial x_k \partial x_k} = \underbrace{\nu \frac{\partial X_m}{\partial x_k} \frac{\partial X_n}{\partial x_k} \frac{\partial^2 A_{ij}}{\partial X_m \partial X_n}}_{A} + \underbrace{\nu \frac{\partial A_{ij}}{\partial X_n} \frac{\partial^2 X_n}{\partial x_k \partial x_k}}_{B(neglected)} \tag{4.7}$$

$$\frac{\partial X_m}{\partial x_k} \frac{\partial X_n}{\partial x_k} = D^{-1}_{mk} D^{-1}_{nk} \tag{4.8}$$

$$\frac{\partial X_m}{\partial x_k}\frac{\partial X_n}{\partial x_k} = (D_{nk}D_{mk})^{-1} \tag{4.9}$$

$$\nu\frac{\partial^2 A_{ij}}{\partial x_k \partial x_k} \approx \nu C_{mn}^{-1}\frac{\partial^2 A_{ij}}{\partial X_m \partial X_n} \tag{4.10}$$

$$\nu\frac{\partial^2 A_{ij}}{\partial x_k \partial x_k} \approx \nu\frac{C_{kk}^{-1}}{3}\delta_{mn}\frac{\partial^2 A_{ij}}{\partial X_m \partial X_n} \tag{4.11}$$

$$\nu\frac{\partial^2 A_{ij}}{\partial x_k \partial x_k} \approx \nu\frac{C_{kk}^{-1}}{3}\frac{\partial^2 A_{ij}}{\partial X_m \partial X_m} \tag{4.12}$$

$$\nu\frac{\partial^2 A_{ij}}{\partial x_k \partial x_k} \approx \nu\frac{C_{kk}^{-1}}{3}\frac{A_{ij}}{(\delta X)^2} \tag{4.13}$$

$$\nu\frac{\partial A_{ij}}{\partial x_k \partial x_k} \approx \frac{C_{kk}^{-1}}{3\tau_\nu}A_{ij} \tag{4.14}$$

where x is the Eulerian position of a particle, initially located at the position X. D is the deformation gradient tensor ($D_{ij} = \frac{\partial x_i}{\partial X_j}$) and C is the right Cauchy-Green tensor ($C = D^T D$). The evolution equation of the deformation gradient tensor (D) is:

$$\frac{dD}{dt} = DA. \tag{4.15}$$

τ_ν is the molecular viscous relaxation time scale, defined as:

$$\tau_\nu = \delta X^2/\nu \approx \lambda_\tau^2/\nu, \tag{4.16}$$

where, λ_τ is Taylor microscale.

The LLDM model of Jeong & Girimaji (2003) uses two major simplifications while dealing with viscous term (A) in equation 4.1:

(i) In Equation 4.11, the inverse Cauchy Green tensor is approximated to be isotropic.
(ii) Term B in equation 4.7 is neglected.

Another possible way of deriving the LLDM model equation 4.14 from equation 4.11 could be through an alternate route by assuming $\frac{\partial^2 A_{ij}}{\partial X_m \partial X_n}$ to be isotropic:

$$\nu\frac{\partial^2 A_{ij}}{\partial x_k \partial x_k} \approx \nu C_{mn}^{-1}\frac{\partial^2 A_{ij}}{\partial X_m \partial X_n}$$

$$\nu\frac{\partial^2 A_{ij}}{\partial x_k \partial x_k} \approx \nu C_{mn}^{-1}A_{ij}\frac{\delta_{mn}}{3(\delta X)^2} \tag{4.17}$$

$$\nu\frac{\partial A_{ij}}{\partial x_k \partial x_k} \approx \frac{C_{kk}^{-1}}{3\tau_\nu}A_{ij} \tag{4.18}$$

The LLDM model has been further used in the enhanced homogenized Euler Equation (EHEE) as well (Suman & Girimaji (2009)). In this work we plan to evaluate the performance of the LLDM model in compressible decaying turbulence using a Lagrangian particle tracker. Using the DNS data, a bunch of fluid particles are chosen at a reference time, and the mean value of the following quantities are calculated following the same set of identified fluid particles:

(i) Exact viscous term: $\left|\nu\frac{\partial A_{ij}}{\partial x_k \partial x_k}\right|$
(ii) LLDM model term: $\left|\frac{C_{kk}^{-1}}{3\tau_\nu}A_{ij}\right|$

In Section 5 we compare the evolutionary history of the exact viscous term and LLDM model term (equation 4.18) directly following a set of identified fluid particles. To identify the influence of compressibility on the evolutionary histories of the exact process and the

Acronyms	$p = 0$	$p < 0$	$p > 0$	Eigenvalues of a_{ij}
SFS	$r < 0$	$r < 0$ & $S2 > 0$	$r < 0$	complex
UFC	$r > 0$	$r > 0$	$r > 0$ & $S2 < 0$	complex
UNSS	$r > 0$ & $q < 0$	$r > 0$	$r > 0$ & $q < 0$	real
SNSS	$r < 0$ & $q < 0$	$r < 0$ & $q < 0$	$r < 0$	real
UFS	—	$r < 0$ & $S2 < 0$	—	complex
UN/UN/UN	—	$r < 0$ & $q > 0$	—	real
SFC	—	—	$r > 0$ & $S2 > 0$	complex
SN/SN/SN	—	—	$q > 0$ & $r > 0$	real

TABLE 2. Zones of various topologies on $p - q - r$ space, where acronyms are: stable-focus-stretching (SFS), unstable-focus-compressing (UFC), unstable-node/saddle/saddle (UNSS), stable-node/saddle/saddle (SNSS), unstable-focus-stretching (UFS), unstable-node/unstable-node/unstable-node (UN/UN/UN), stable-focus-compressing (SFC), stable-node/stable-node/stable-node (SN/SN/SN).

model, we examine the statistics of these quantities conditioned on (i) initial dilatation-level and initial topology of fluid particles. We also examine the eigenvalues of C^{-1} and $\frac{\partial^2 A_{ij}}{\partial X_m \partial X_n}$ tensor. These eigenvalues are sorted in the order $\alpha > \beta > \gamma$. Since our focus is to examine whether the isotropic assumption of C^{-1} and $\frac{\partial^2 A_{ij}}{\partial X_m \partial X_n}$ is realistic or not, we examine the statistics of self-normalized eigenvalues:

$$R_\alpha = \overline{\frac{|\alpha|}{\sqrt{\alpha^2 + \beta^2 + \gamma^2}}}$$
$$R_\beta = \overline{\frac{|\beta|}{\sqrt{\alpha^2 + \beta^2 + \gamma^2}}}$$
$$R_\gamma = \overline{\frac{|\gamma|}{\sqrt{\alpha^2 + \beta^2 + \gamma^2}}} \quad (4.19)$$

Like our previous works (Suman & Girimaji (2010*a*); Danish *et al.* (2016*a*); Parashar *et al.* (2017*a*)), the following locally normalized form of the dilatation-rate is used:

$$a_{kk} = A_{kk}/\sqrt{A_{ij}A_{ij}}. \quad (4.20)$$

The normalized dilatation-rate of a fluid particle (henceforth, referred to as just "dilatation") represents the normalized rate of change in density of a local fluid particle:

$$\frac{1}{\rho}\frac{d\rho}{dt'} = \frac{1}{\rho}\left[\frac{\partial \rho}{\partial t'} + V_k \frac{\partial \rho}{\partial X_k}\right] = -a_{ii} \quad (4.21)$$

where $dt' = dt\sqrt{A_{ij}A_{ij}}$ represents time normalized with the local magnitude of the velocity gradient tensor itself.

The topology of a fluid particle is the local streamline pattern as observed with respect to a reference frame which is translating with the centre of mass of the fluid particle. The topology of a fluid particle depends on the nature of eigenvalues of the velocity gradient tensor. However, it can also be inferred with the knowledge of the three invariants of the

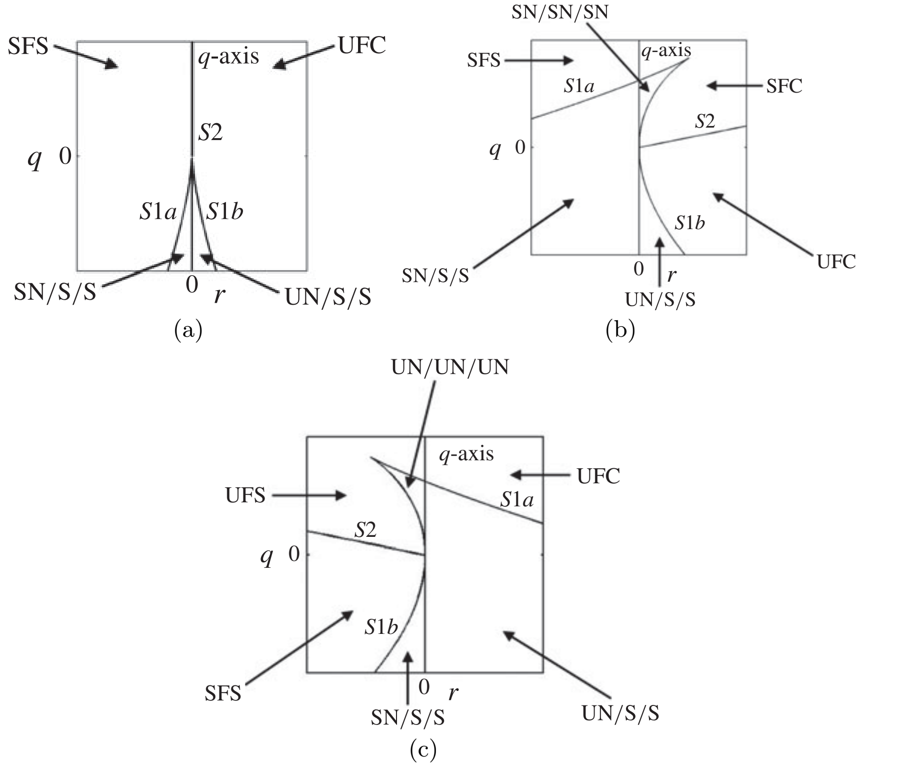

FIGURE 2. Flow topologies represented in different p-planes: a) $p = 0$, b) $p > 0$ and c) $p < 0$. (Figures to be reproduced with permission from Suman & Girimaji (2010*a*).)

velocity gradient tensor P, Q, R:

$$P = -A_{ii}, Q = \frac{1}{2}\left(P^2 - A_{ij}A_{ji}\right), and$$
$$R = \frac{1}{3}\left(-P^3 + 3PQ - A_{ij}A_{jk}A_{ki}\right). \tag{4.22}$$

The normalized invariants (p,q,r) of the local velocity gradient tensor (a) are defined as:

$$p = -a_{ii}, q = \frac{1}{2}\left(p^2 - a_{ij}a_{ji}\right), and$$
$$r = \frac{1}{3}\left(-p^3 + 3pq - a_{ij}a_{jk}a_{ki}\right). \tag{4.23}$$

Determination of the topology of a fluid particle can also be done using the invariants of the normalized velocity gradient tensor (a). Chen *et al.* (1989) categories topological patterns (Table 2) that can be observed in an incompressible field into UNSS, SNSS, SFS, UFC. In compressible flows additional four more topologies can exist: SFS and SNSNSN in contracting fluid particles and UFS and UNUNUN in expanding fluid particles. Figure 2 shows different topologies existing in different p-planes in p-q-r space. Figure 3 present schematics of these topological patterns.

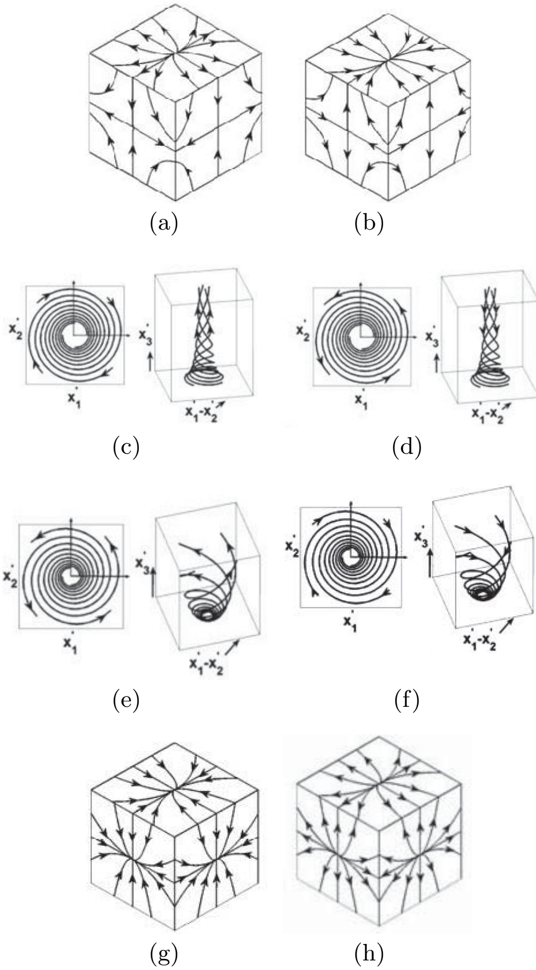

FIGURE 3. Flow patterns corresponding to different flow topologies: a) UNSS, b) SNSS, c) SFS, d) UFC, e) UFS, f) SFC, g) SNSNSN and h)UNUNUN. (Figures to be reproduced with permission from Suman & Girimaji (2010*a*).)

4.2. *Part II*

Since the value of three invariants of the velocity gradient tensor uniquely determines the topology associated with the local fluid particle, the dynamics of topology can be studied in terms of the dynamics of invariants themselves. Using the evolution equation of the velocity-gradient-tensor (Equation 2.7), the time-evolution of invariants (P,Q,R) of the velocity-gradient-tensor A can be found out (Bechlars & Sandberg (2017)):

$$\begin{aligned}\frac{dP}{dt} &= P^2 - 2Q - S_{ii},\\ \frac{dQ}{dt} &= QP - \frac{2P}{3}S_{ii} - 3R - A_{ij}S^*_{ji},\\ \frac{dR}{dt} &= -\frac{Q}{3}S_{ii} + PR - PA_{ij}S^*_{ji}) - A_{ik}A_{kj}S^*_{ji} \qquad (4.24)\end{aligned}$$

where, S is the source term in the evolution equation of velocity-gradient-tensor

(Equation 2.7) and S^* is the traceless part of S tensor defined as:

$$
\begin{aligned}
S &= -\mathbb{P} + \Upsilon, \\
S^* &= S - \frac{S_{kk}}{3}.
\end{aligned}
\tag{4.25}
$$

Here $\mathbb{P}$ is the pressure hessian tensor and Υ represents the contribution of viscosity in the evolution equation of the velocity-gradient tensor (A), as shown in Equation 2.7. The relation between non-normalized invariants (P,Q,R) and normalized invariants (p,q,r) is shown in equation 4.26:

$$
\begin{aligned}
p &= \frac{P}{\sqrt{A_{ij}A_{ij}}}, \\
q &= \frac{Q}{A_{ij}A_{ij}}, \\
r &= \frac{R}{(A_{ij}A_{ij})^{3/2}}
\end{aligned}
\tag{4.26}
$$

Subsequently, using equations (4.24 & 4.26), the evolution equation of normalized invariants (p,q,r) can be derived:

$$
\begin{aligned}
\frac{dp}{dt} = \frac{d}{dt}\left(\frac{P}{\sqrt{A_{ij}A_{ij}}}\right) &= \frac{1}{\sqrt{A_{ij}A_{ij}}}\frac{dP}{dt} - \frac{P}{(A_{ij}A_{ij})^{3/2}}A_{ij}\frac{dA_{ij}}{dt}, \\
\frac{dq}{dt} = \frac{d}{dt}\left(\frac{Q}{A_{ij}A_{ij}}\right) &= \frac{1}{A_{ij}A_{ij}}\frac{dQ}{dt} - \frac{2Q}{(A_{ij}A_{ij})^{2}}A_{ij}\frac{dA_{ij}}{dt}, \\
\frac{dr}{dt} = \frac{d}{dt}\left(\frac{R}{(A_{ij}A_{ij})^{3/2}}\right) &= \frac{1}{(A_{ij}A_{ij})^{3/2}}\frac{dQ}{dt} - \frac{3R}{(A_{ij}A_{ij})^{5/2}}A_{ij}\frac{dA_{ij}}{dt}.
\end{aligned}
\tag{4.27}
$$

While following a fluid particle in physical space and storing its velocity gradient tensor information, we can indirectly track the p-q-r location of the fluid particle. We refer to such a trajectory as the exact Lagrangian trajectory (ELT) of an individual fluid particle. Mean Lagrangian trajectory (MLT) can be obtained by tracking the mean position of a selected number of particles originating from the same location in p-q-r space (within the specified tolerance) at some reference time (t_{ref}). This procedure involves no approximation while calculation of trajectories of fluid particles in p-q-r space.

As mentioned before, many researchers have adopted an alternate though approximate procedure of examining trajectories in the p-q-r space. This alternative method does not track the individual fluid particles, but use the averaged value of the RHS of Equation 4.27 conditioned on a chosen set of p,q,r. In this method, a one-time Eulerian dataset of the flow field is used. The statistics thus obtained are essentially the conditional averages of the rate of change of the invariants with the conditional parameters being the local value of p,q,r in the p-q-r space. The trajectories thus obtained are basically instantaneous streamlines in p-q-r space referred to as the conditional mean trajectories (CMT).

In Section 6 we first investigate dynamics of topology in compressible turbulence employing the method of CMT. For plotting all CMTs we employ the flow field obtained from different simulations at a time instant when velocity derivative skewness has settled i.e. $S_u \in (-0.6, -0.4)$. A bin size of $r \in \overline{r} \pm 0.01$ and $q \in \overline{q} \pm 0.025$ is taken to compute all CMTs. In §6.1 we present a comparison of CMT and MLT and identify the constraints of the former. Subsequently in §6.2 we employ exact ELTs to estimate lifetime of various topologies in compressible turbulence.

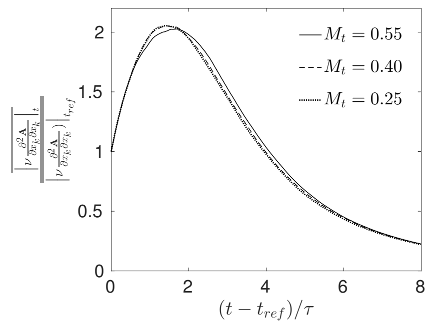

FIGURE 4. Mach number dependence on evolution of exact viscous term ($t_{ref} = 0.5\tau$).

5. Lagrangian Evolution of deformation gradient tensor

We first analyze the evolution of the exact viscous term in §5.1. After understanding the evolution characteristics of the exact viscous term, we then compare the performance of the LLDM model term in approximating the exact viscous process in §5.2.

5.1. *Analysis of the evolution of the exact viscous term*

We first present the time evolution of the Lagrangian statistics of the exact viscous diffusion process $\left(\left|\nu \frac{\partial A_{ij}}{\partial x_k \partial x_k}\right|\right)$ from simulations B-D in Figure 4. All these simulations differ in terms of the initial Mach number. In each of these simulations, the exact viscous process shows a two-stage evolution. In the first stage of evolution, $\left(\overline{\left|\nu \frac{\partial A_{ij}}{\partial x_k \partial x_k}\right|}\right)$ increases and reaches a peak value. In the second stage, it decays in magnitude. This evolution is reminiscent of the evolution of dissipation itself. Indeed the time instant of the peak of dissipation and that of the viscous process match ($t_{peak-dissipation} = 2\tau$). The amplification in the first stage can be attributed to steepening of gradients due to the rapid spread of the spectrum. The decay in the second stage of evolution can be attributed mainly to the decay in kinetic energy. Comparing the curves from these three simulations it is clear that initial Mach number has little negligible influence on the evolution of viscous diffusion term $\left(\overline{\left|\nu \frac{\partial A_{ij}}{\partial x_k \partial x_k}\right|}\right)$. Such behavior is analogous to the variation in dissipation rate ($\epsilon = \nu \overline{A_{ij} A_{ij}}$) with varying M_t, which has been shown to be negligible by Samtaney *et al.* (2001). The viscous diffusion term is basically a higher order derivative of the dissipation rate. Hence such behaviour is in line with previously observed behaviour for dissipation rate.

To further understand the influence of compressibility on the viscous process, we present the results conditioned on dilatation. In Figure 5a we present results conditioned on negative dilatation levels. Similarly in Figure 5b we present results conditioned on positive levels of dilatation. All the results are from the Simulation C (Table 1). It can be observed from Figure 5 that the intensity of viscous process is elevated at higher dilatation levels (+/-). This is attributed to the higher gradients of velocity gradient tensor for highly contracting and expanding fluid particles.

In Figure 6 we present results conditioned on initial flow topology. It can be observed that the rotation based topologies (SFC, UFS, UFC, SFS) tend to show higher growth rate in the first phase of evolution, reaching higher peaks as compared to strain-dominated topologies (UNSS and SNSS). SFC topology shows the highest growth rate as compared to all other topologies.

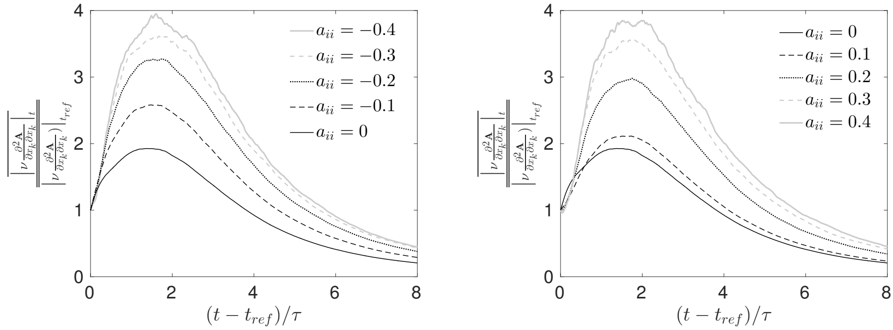

(a) (b)

FIGURE 5. Dependence of dilatation rate on evolution of exact viscous term ($t_{ref} = 0.5\tau$).

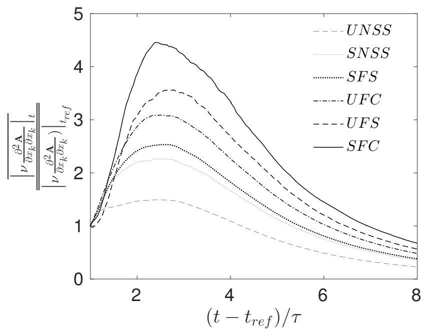

FIGURE 6. Dependence of topology on evolution of exact viscous term ($t_{ref} = 0.5\tau$).

5.2. *Evaluation of the LLDM model*

Having examined the behaviour of the exact process following fluid particles, now we examine the performance of the LLDM model of Jeong & Girimaji (2003), which intends to capture the essential physics of the exact process. For this examination, we use the results of Simulation C, but instead of computing the exact viscous process $\left(\overline{\left|\nu \frac{\partial A_{ij}}{\partial x_k \partial x_k}\right|}\right)$, we compute the mean value of the magnitude of the LLDM model term $\left(\overline{\left|\frac{C_{kk}^{-1}}{\tau_\nu}\mathbf{A}\right|}\right)$ following the same set of fluid particles which were selected for computing statistics of the exact process. In Figure 7, we compare the LLDM model with the exact viscous term. We observe that unlike the evolution of the exact process, the LLDM model term shows monotonic growth with time. At the early stages of evolution, the monotonic growth is at least qualitatively the same as the exact process. However, at later stages (after the dissipation peak event) this continued monotonic growth in is gross disagreement with the decaying behaviour of the exact process after reaching a peak value. In Figure 8 we present the evolution of $|A|$ with time. We observe that $|A|$ does show a two-stage behaviour and starts decaying after the peak dissipation event. Comparing Figure 7 and Figure 8, it is clear that the coefficient C_{kk}^{-1} of the LLDM model grossly overestimates the influence of the C^{-1} tensor.

To better understand the reason for the failure of the LLDM model, we revisit the modelling assumptions. One of the assumptions used in the model is that the tensor C^{-1} is isotropic. To scrutinize whether this assumption is contributing to the model failure,

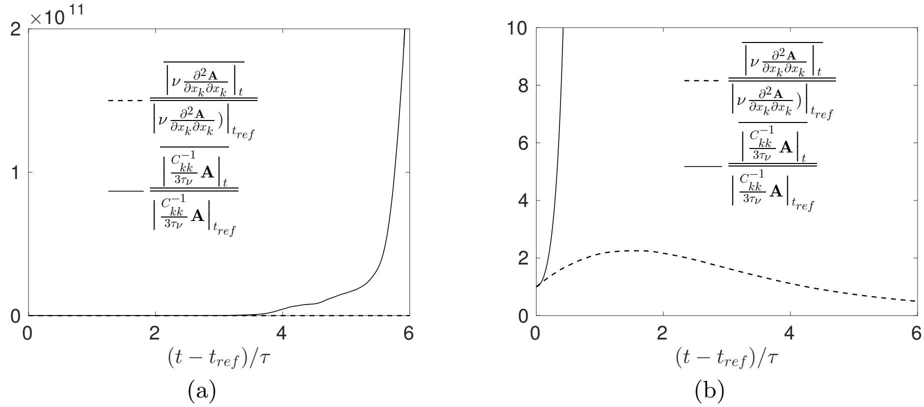

FIGURE 7. Comparison of LLDM model term and the exact viscous term: a) unscaled axis, b) axis scaled to visualize the difference in growth rates of the two processes.

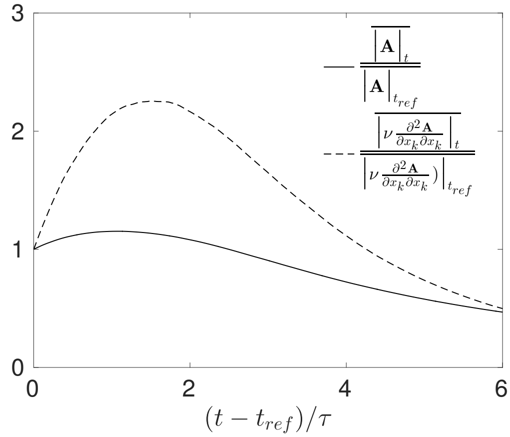

FIGURE 8. Evolution of magnitude of velocity gradient tensor $|A|$.

we examine the eigenvalues of the C^{-1} tensor. The C^{-1} tensor is always symmetric (since $C = DD^T$ is symmetric), hence the eigenvalues of C^{-1} are always real. To examine the validity of the isotropic assumption, we plot the mean evolution of the three eigenvalues $(\alpha > \beta > \gamma)$. In Figure 9 we present the Lagrangian statistics of R_α, R_β and R_γ as a function of time. We observe that the eigenvalues begin to depart from each other. R_α increases appreciably during the evolution phase, while R_β and R_γ decreases to negligible values. This indicates that the C^{-1} tensor is strongly biased towards $\alpha-$eigenvector. Thus, it is clear that the assumption of the isotropy of the tensor is incorrect.

As shown in §4, (Equation 4.17 and 4.18) viscous term in LLDM model can also be recovered by assuming the 4^{th} order tensor $\frac{\partial^2 A_{ij}}{\partial X_m \partial X_n}$ to be isotropic. However, it is not possible to find the eigen-values of this tensor directly. By lagrangian change of variables, $\frac{\partial^2 A_{ij}}{\partial X_m \partial X_n}$ can be approximated as:

$$\frac{\partial^2 A_{ij}}{\partial X_m \partial X_n} \approx \frac{x_m}{X_m} \frac{x_n}{X_n} \frac{\partial^2 A_{ij}}{\partial x_m \partial x_n} \tag{5.1}$$

Since a product of an anisotropic tensor with an isotropic tensor is always anisotropic,

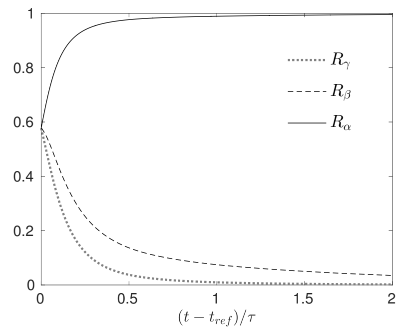

FIGURE 9. Evolution of locally normalized eigenvalues of C^{-1}

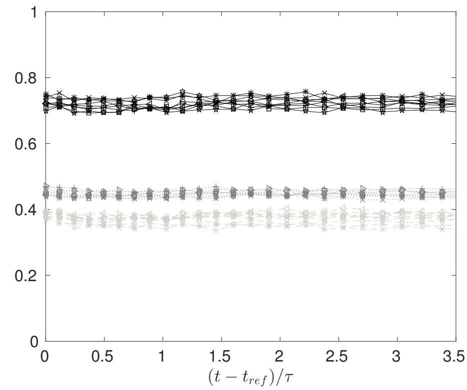

FIGURE 10. Evolution of locally normalized real part of eigenvalues of $\frac{\partial^2 A_{ij}}{\partial x_m \partial x_n}$. Three different colors of the line plot viz. black, light gray, dark gray represents R_α, R_β and R_γ respectively. Different markers represents eigenvalues corresponding to different 2^{nd} order tensors (components) of the original 4^{th} order tensor. R_{ij} represents ratio of normalized eigenvalue for $\frac{\partial^2 A_{ij}}{\partial X_m \partial X_n}$. Different marker identifiers are $\longrightarrow$ +: R_{11}, o: R_{12}, $*$: R_{13}, <: R_{21}, >: R_{22}, x: R_{23}, □: R_{31}, ⬡: R_{32}, ⬠: R_{33}

we rather evaluate the eigenvalues of $\frac{\partial^2 A_{ij}}{\partial x_m \partial x_n}$ tensor. Since, this tensor is of order 4, we dissociate the tensor into 9 second-order tensors and analyze their eigenvalues. Since, $\frac{\partial^2 A_{ij}}{\partial x_m \partial x_n}$ is not symmetric, it is not guaranteed to have real eigenvalues. Indeed, the eigenvalues of the tensor are not purely real with mean ratio of the imaginary part to the real part for α, β and γ eigenvalues to be 0.13, 0.77 and 0.17 respectively . However, inorder to measure the extent of anisotropy, we plot the ratio of real part of the eigenvalues in terms of R_α, R_β and R_γ in Figure 10. Clearly the $\frac{\partial^2 A_{ij}}{\partial x_m \partial x_n}$ tensor is anisotropic with ratio of the eigenvalues as: $\alpha : \beta : \gamma :: 1.9 : 1.0 : 1.1$. Hence, it can be concluded that the $\frac{\partial^2 A_{ij}}{\partial X_m \partial X_n}$ tensor is also anisotropic.

In summary, our investigations reveal that the performance of the LLDM model is unrealistic in the later stage of evolution of decaying turbulence. In the first stage of evolution, even though qualitatively LLDM captures the right behaviour, it tends to overestimate the value. Our investigations reveal that the isotropy assumption of the C^{-1} and $\frac{\partial^2 A_{ij}}{\partial X_m \partial X_n}$ tensor is one of the major cause of the unrealistic behaviour of the LLDM model term as compared to the exact viscous term.

	100% UNSS				100% SNSS				100% SFS				100% UFC			
	UNSS	SNSS	SFS	UFC	UNSS	SNSS	SFS	UFC	UNSS	SNSS	SFS	UFC	UNSS	SNSS	SFS	UFC
t_{ref}	100	0	0	0	0	100	0	0	0	0	100	0	0	0	0	100
$t_{ref}+3\tau$	27	8	38	26	27	8	39	26	23	7	41	28	26	8	39	27

TABLE 3. Percentage topology composition for particles after 3 eddy-turnover time starting with 100% UNSS, SNSS, SFS and UFC sample respectively.

6. Comparisons of Eulerian and Lagrangian investigations of flow field topology

In §6.1 we present a comparative study between the CMT and MLT and highlight some important differences between the two. Further in the §6.2 we study the life of topology using ELTs and examine the influence of compressibility on it.

6.1. *CMT vs. MLT*

CMT has been extensively used as a method to predict particle trajectories in p-q-r space. CMTs are basically instantaneous streamlines of particles in p-q-r space. Several researchers have drawn conclusions based on the time-integrated behaviour of CMT as a complete substitute of MLT. However, using CMT for predicting long-term behaviour−such as finding the life of topology may not be as accurate as MLT. We present a discussion here highlighting the shortcomings of CMT over MLT. As most of the CMT based studies have been performed for incompressible flows (Ooi *et al.* (1999); Meneveau (2011); Lozano-Durán *et al.* (2015)), we use nearly incompressible simulation (case A 1), to demonstrate the difference between CMT and MLT. We further condition the data-set at very small dilatation value ($|a_{ii}| < 0.01$) to assert very weak compressibility effects.

To highlight the difference, we show CMT and MLT emerging from a small region in q-r plane ($p = 0 \pm 0.01$) in Figure 11(a-d) (for all four topologies that exist in this plane). It is evident from Figure 11 that the instantaneous CMT does not coincide with the MLT of fluid particles in q-r plane. There is no directional preference of fluid particles to rotate in spiral order and converge to the origin of q-r plane, as inferred by CMT (Figure 11(a-d)). In-fact the mean trajectory (MLT) converging directly to origin with no tendency to rotate around the origin, explains no directional preference and a clear tendency to randomly move in the q-r space. This argument is further supported by Figure 12(a), where the root-mean-squared value of q and r is plotted with time.

Using the CMT approach, it can be shown that in around 3 eddy-turnover time, a fluid particle completes one complete rotation around the origin (Ooi *et al.* (1999)). However, it can be clearly seen in Figure 12(a), that in just 1 eddy-turnover time, the rms approaches its maximum value ($q_{rms} \approx 0.24$ and $r_{rms} \approx 0.05$), indicating maximum spread of the fluid particles in q-r plane. In-fact these RMS values are identical to the RMS of q and r location of global unconditioned sample. To further understand this difference, we plot the location of various fluid particles starting from a small region in q-r plane after 1 eddy-turnover time (Figure 12(b)). It can be observed that the population spread after 1 eddy-turnover time, is in-fact similar to the global spread of particles in q-r plane with major concentration along the Vieillefosse tail.

Table 3 shows the percentage topology composition after 3 eddy-turnover times of particles initially belonging to a distinct topology. It is evident that after 3 eddy-turnover times the particles gets distributed throughout the q-r plane with the final composition identical to global unconditioned sample. In fact, the composition after 3 eddy-turnover times is approximately equal to the global topology composition for

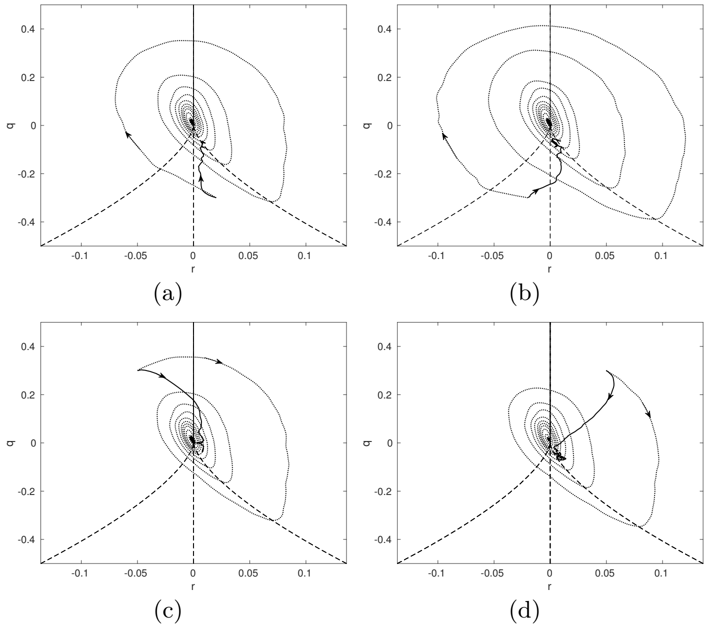

FIGURE 11. Comparison of instantaneous CMTs (dotted line) and actual mean Lagrangian trajectory MLT (solid line) of fluid particles with bin dimensions $r \in \overline{r} \pm 0.01$ and $q \in \overline{q} \pm 0.025$ for (a)UNSS, (b)SNSS, (c)SFS and (d)UFC topology. Dashed lines represent surfaces: S1a, S1b and S2.

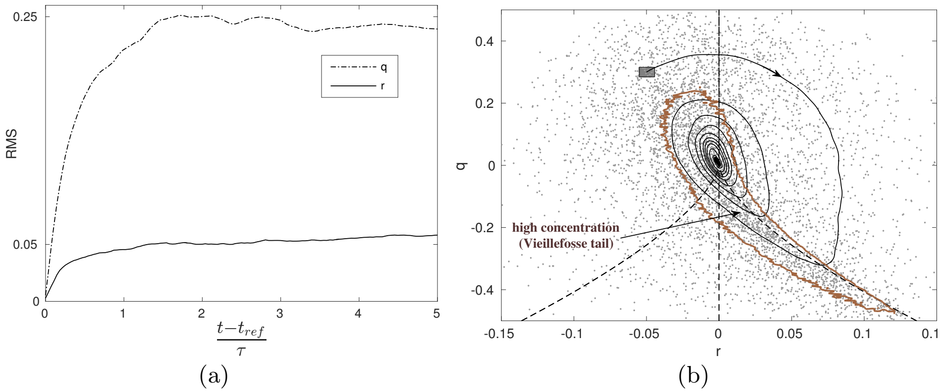

FIGURE 12. (a) Evolution of root mean squared value of invariants q and r starting from a bounded region r (-0.05 ± 0.01) and q (0.3 ± 0.025) (b) Instantaneous CMT (solid line) and final spread of Lagrangian particles after 1 eddy-turnover time starting from the bounded region. Sample size of conditioned particles in the bounded region ≈ 5000.

isotropic incompressible flow as reported by Suman & Girimaji (2009). This observation challenges the CMT approach that approximates particle motion in the q-r plane using instantaneous Eulerian flow field. Table 4 shows anticlockwise and clockwise movement of particles starting from a particular topology using ELT approach. It can be seen that a significant fraction of particles moves anti-clockwise (1/2 for SNSS topology and 1/3 for UNSS, SFS and UFC topology). Therefore it can be concluded that the CMT approach inaccurately predicts cyclic rotation of particles around the origin.

Hence, from the above analysis, we conclude that CMT does not represent actual

	UNSS	SNSS	SFS	UFC
% anticlockwise	32	51	33	33
% clockwise	68	49	67	67

TABLE 4. Clockwise and anti-clockwise movement of particles in q-r plane. [Note: This table shows percentage transfer of particles. The topology composition remains invariant with time i.e. Total particles moving in and out of a particular topology is same.]

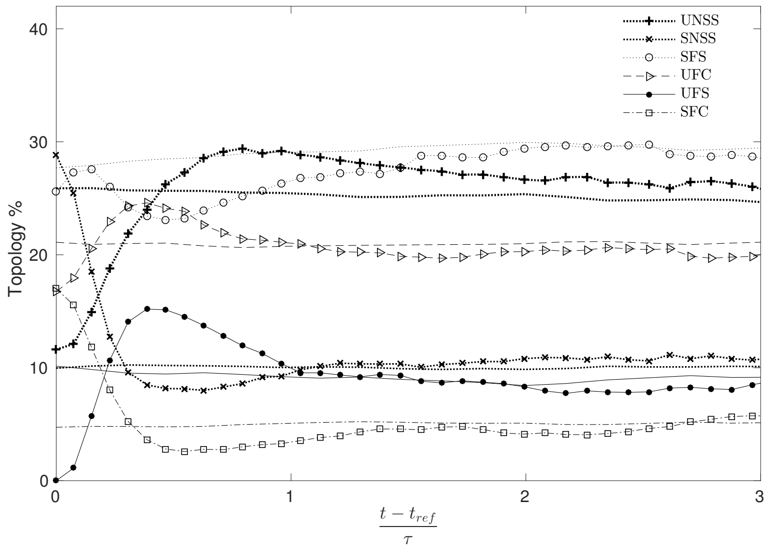

FIGURE 13. Evolution of topology-composition for particles initially conditioned at $p = +0.5 \pm 0.05$ for 6 major topologies viz. UNSS, SNSS, SFS, UFC, UFS, SFS (Simulation E). Initial composition at $t_{ref} = 4\tau$: UNSS = 11.6%, SNSS = 28.9%, SFS = 25.6%, UFC = 16.7%, UFS = 0%, SFC = 17.0%, SNSNSN = 0.2%, UNUNUN = 0%. Lines without markers represents topology composition of global unconditioned sample.

motion of fluid particles in q-r plane for incompressible flow. In general, the fluid particles move around randomly in q-r plane, such that at every time instant the overall distribution of particles is identical, with major concentration along the Vieillefosse tail.

Although, the above analysis is performed for incompressible flow, we expect even for compressible flow, the motion of fluid particles to be such that their topology composition approach global topology composition with time. To prove this hypothesis, we show time-evolution of percentage composition of particles originating from a discrete p-plane ($p = +0.5 \pm 0.05$) for compressible simulation E (Table 1) in Figure 13. It can be seen in Figure 13 that despite a significant variation in initial composition of topology as compared to global composition, the particles moves around randomly in p-q-r space such that their percentage composition tends toward the global composition.

6.2. *Life of topology*

In this section, we quantify the life-time of existence of particles in different topologies. Starting with 10,00,000 particles, we tag the particles based on their topology at t_{ref} and track them until they lose their initial topology. The life-time of each particle (l_κ) in a particular topology is measured as a fraction of Kolmogorov time, τ_κ (measured at t_{ref}), calculated by recording the time from t_{ref} to the instant the particle loses it's initial

	UNSS	SNSS	SFS	UFC
Sample %	25.2	5.4	43.5	25.9
Life of topology (κ_τ)	1.80	0.53	3.32	2.08
Life %	23.32	6.86	42.95	26.91

TABLE 5. Life of topology L_κ for nearly incompressible flow (case A). The sample is further conditioned on dilatation ($|a_{ii}| < 0.01$) to ensure strong incompressibility. Sample size ≈ 1,25,000 particles (conditioned).

topology. Further, we calculate the life-time of topology (L_κ) as the mean life-time of all the particles in a particular topology (in terms of τ_κ):

$$L_\kappa = \sum_{i=1}^{N} \frac{l_{\kappa_i}}{N} \tag{6.1}$$

6.2.1. *Incompressible flow*

We first show life of topology for nearly incompressible simulation (case A) in Table 5. To assert very mild compressibility, we further condition our sample on dilatation ($|a_{ii}| = |p| < 0.01$). It can be observed that life of topology is proportional to the percentage composition of topology. SFS topology is the most stable with average lifetime of $3.3\kappa_\tau$, next is the UFC topology with average lifetime of $2\kappa_\tau$, next most stable is UNSS with a lifetime of $1.8\kappa_\tau$. SNSS topology is found to be least stable with average lifespan of $0.5\kappa_\tau$. Hence, for incompressible flow, the order of stability of topology is as follows:

$$SFS \longrightarrow UFC \longrightarrow UNSS \longrightarrow SNSS.$$

Table 6 shows the average velocity ($|U_{pqr}| = |\frac{\partial p}{\partial t}\hat{p} + \frac{\partial q}{\partial t}\hat{q} + \frac{\partial r}{\partial t}\hat{r}|$) of particles in different topologies in p-q-r space. It is interesting to observe that although the average velocity for different topologies is comparable in magnitude, there is a significant difference in their lifetimes (L_κ). It can also be seen in Table 5, that the proportion of life of different topologies is identical to their percentage composition. To explain the variation in L_κ for different topologies, we focus on the distribution of the population in various zones of topology rather than just percentage composition. Figure 14 shows region of high concentration of particles in q-r plane. This region of high particle concentration is also termed "Vieillofosse tail". It can be seen in Figure 14 that, while SFS and UFC region have an equal area in the q-r plane, their population distribution is not alike. In UFC, the population has a spread closer to the surfaces of unlike topologies, than for SFS topology. Closer proximity to the nearby surfaces of unlike topologies explains the likelihood of UFC to be more prone to change than SFS topology, having known that their average speeds in p-q-r space are comparable in magnitude (Table 6). Similarly, UNSS and SNSS have equal area, still, UNSS is found to be more stable than SNSS topology. This is because for SNSS topology the bulk of the population is found closer to the origin where nearby surfaces separating different topologies are closer leading to higher probability of particles crossing the zone of SNSS topology into other topologies. However, in UNSS topology, the population although highly concentrated near the origin, has significant population spread away from the origin, where nearby surfaces for interconversion are not very close. Hence, despite having comparable average velocities, different topologies have different lifetimes (L_κ).

	UNSS	SNSS	SFS	UFC
average velocity $\|U_{qr}\|$ (units: s^{-1})	0.23	0.28	0.23	0.26

TABLE 6. Average velocity of particles in p-q-r space ($U_{pqr} = \frac{\partial p}{\partial t}\hat{p} + \frac{\partial q}{\partial t}\hat{q} + \frac{\partial r}{\partial t}\hat{r}$) for simulation case A.

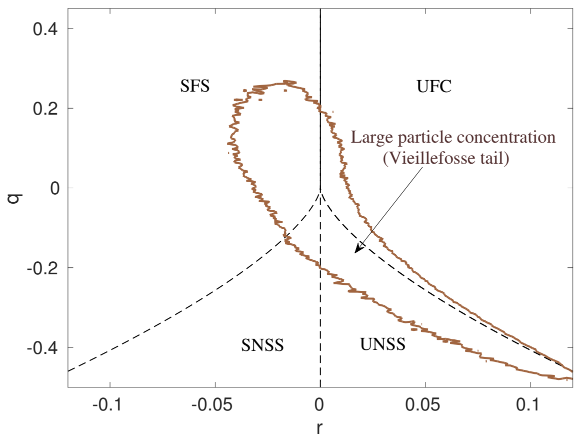

FIGURE 14. Region of high concentration of particles in q-r space.

6.2.2. *Compressible flow*

We show average life-time of topology for compressible simulations (case E-I) in Table 7. It can be seen that the life-time of topology is again a strong function of particle concentration. In-fact the percentage life of different topologies is almost identical to the composition of their populations (Table 7). However, the order of stability seems to be influenced by M_t (Table 7). For weakly compressible flow (simulation A), the order of stability based on lifetime for 4 major topologies is $SFS \longrightarrow UNSS \longrightarrow UFC \longrightarrow SNSS$. However, global turbulent Mach number of the flow seems to affect the order of stability.

To explain this variation in the order of stability with M_t, we now focus on the localized origin of compressibility. As shown by Suman & Girimaji (2010*a*), the extent of compressibility can be determined solely by the strength of dilatation ($-\sqrt{3} < a_{ii} < \sqrt{3}$). Compressibility is a localized phenomenon i.e. regions of weak and strong compressibility are present in the flow field. However, statistically, by looking at the probability-density-function (PDF) of dilatation one can determine the extent of compressibility. A larger spread of the dilatation PDF, represent a high strength of compressibility. For incompressible flow ($a_{ii} = -p \approx 0$), only 4 flow topologies exist viz. UNSS, SNSS, SFS and UFC topology. But compressibility gives rise to new flow-topologies (Figure 2), existing in p-q-r space in planes of non-zero dilatation ($|p| > 0$). The population of these topologies depend upon the spread of dilatation. Weak compressibility, accompanied by low dilatation spread leads to a low population of topologies existing in non-zero p-planes and vice-versa for highly compressible flow. In Figure 15, we show the PDF of dilatation for different simulations. It can be seen that the dilatation spread increases with turbulent Mach number, however, there seems to be little to no dependence on Reynolds number as evident from simulations F-H (Figure 15).

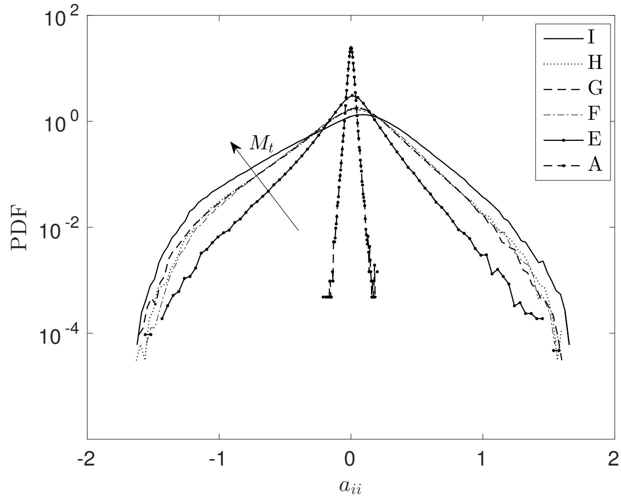

FIGURE 15. PDF of noramilized dilatation a_{ii} for different simulations (Table 1).

From the above discussion, it can be concluded that there is no general order of stability of topology for compressible flows. However, for major 4 topologies (UNSS, SNSS, SFS and UFC), there is a particular order of stability:

$$SFS \longrightarrow UNSS \longrightarrow UFC \longrightarrow SNSS.$$

Further, at very high Mach numbers the order stability based on life-time of existence is found to be as follows:

$$SFS \longrightarrow UNSS \longrightarrow UFC \longrightarrow UFS \longrightarrow SNSS \longrightarrow SFC \longrightarrow UNUNUN \longrightarrow SNSNSN.$$

In order to explain the variation of lifetime of topology with M_t, we report the magnitude of mean velocities ($U_{pqr} = \frac{\partial p}{\partial t}\hat{p} + \frac{\partial q}{\partial t}\hat{q} + \frac{\partial r}{\partial t}\hat{r}$) of particles in p-q-r space in Table 8. It can be seen that $|U_{pqr}|$ increases with M_t for all major topologies, while for extreme topologies−UNUNUN and SNSNSN, the variation in $|U_{pqr}|$, although most likely opposite, seems less significant as compared to variation in rest of the 6 topologies.

For first 4 topologies (UNSS, SNSS, SFS, UFC), the decrease in life with increasing M_t can be attributed to the increase in $|U_{pqr}|$ with increasing M_t. The rest of the topologies come into existence only at high M_t, hence first their lifetime increases with M_t, but further, with an increase in M_t their lifetime tend to remain constant, despite variation in U_{pqr}.

Further, as can be inferred from simulations F-H in Table 7, the Reynolds number show negligible influence on the lifetime/stability of topology.

Simulation		UNSS	SNSS	SFS	UFC	UFS	SFC	SNSNSN	UNUNUN
case A	Sample %	25.2	5.4	43.5	25.9	0	0	0	0
M=0.075	Life of topology	1.80	0.53	3.32	2.08	0	0	0	0
R = 70	Life %	23.32	6.86	42.95	26.91	0	0	0	0
case E	Sample %	24.68	8.35	33.78	21.67	5.17	4.53	0.09	0.09
M=0.6	Life of topology (κ_τ)	1.31	0.44	1.80	1.15	0.28	0.24	0.05	0.05
Re=350	Life %	24.62	8.27	33.83	21.62	5.26	4.51	0.01	0.01
case F	Sample %	27.81	10.26	28.42	20.88	8.44	3.89	0.14	0.15
M=1	Life of topology (κ_τ)	1.04	0.31	1.13	0.85	0.35	0.24	0.06	0.11
Re=150	Life %	25.43	7.58	27.63	20.78	8.56	5.87	1.47	2.69
case G	Sample %	26.61	9.82	26.26	21.50	8.39	4.14	0.14	0.14
M=1	Life of topology (κ_τ)	1.01	0.31	1.18	0.86	0.35	0.25	0.06	0.10
Re=100	Life %	24.51	7.52	28.64	20.87	8.50	6.07	1.46	2.43
case H	Sample %	26.52	9.45	29.96	21.52	8.08	4.23	0.13	0.10
M=1	Life of topology (κ_τ)	1.00	0.29	1.20	0.86	0.33	0.24	0.06	0.08
Re=70	Life %	24.63	7.14	29.56	21.18	8.13	5.91	1.48	1.97
case I	Sample %	26.07	10.10	27.44	21.16	10.49	4.32	0.23	0.21
M=1.5	Life of topology (κ_τ)	0.87	0.26	0.94	0.74	0.35	0.23	0.07	0.09
Re=70	Life %	24.51	7.32	26.48	20.85	9.86	6.48	1.97	2.54

TABLE 7. Life of topology for compressible flows (case A, E-I). Sample size = 10,00,000 particles.

Simulation	UNSS	SNSS	SFS	UFC	UFS	SFC	SNSNSN	UNUNUN
A	0.23	0.28	0.23	0.26	-	-	-	-
E	0.58	0.88	0.60	0.66	0.62	0.96	2.6	1.80
F	0.86	1.39	0.95	1.00	0.82	1.55	2.15	1.33
G	0.84	1.35	0.92	0.99	0.80	1.49	2.35	1.21
H	0.88	1.37	0.97	1.03	0.87	1.46	1.87	1.37
I	1.01	1.57	1.13	1.18	0.90	1.76	1.94	1.27

TABLE 8. Average velocity of particles in p-q-r space ($|U_{pqr}| = |\frac{\partial p}{\partial t}\hat{p} + \frac{\partial q}{\partial t}\hat{q} + \frac{\partial r}{\partial t}\hat{r}|$) for simulations A and E-I.

6.2.3. *Influence of initial dilatation*

In Figure 16, we present the variation in L_κ for various topologies with initial dilatation (a_{ii}). To explain the variation in L_κ with dilatation we show joint-PDF (JPDF) of particle population in different planes of discrete dilatation in Figure 17. For UNSS topology, peak life-times (L_κ) are observed at 0 dilatation (Figure 16(a)). Particles with UNSS topology having initial positive dilatation have higher life as compared to those with initial negative dilatation. This happens because for UNSS topology, the zone of existence in p-q-r space shrinks along with decrease in population as dilatation decreases from high positive dilatation to negative dilatation as shown in figure 17 (b-f). On the contrary, the region of existence of SNSS topology widens while moving from high positive to high negative population (17 (b-f)). This leads to lower population of SNSS topology at high positive dilatations (Figure 16(b)).

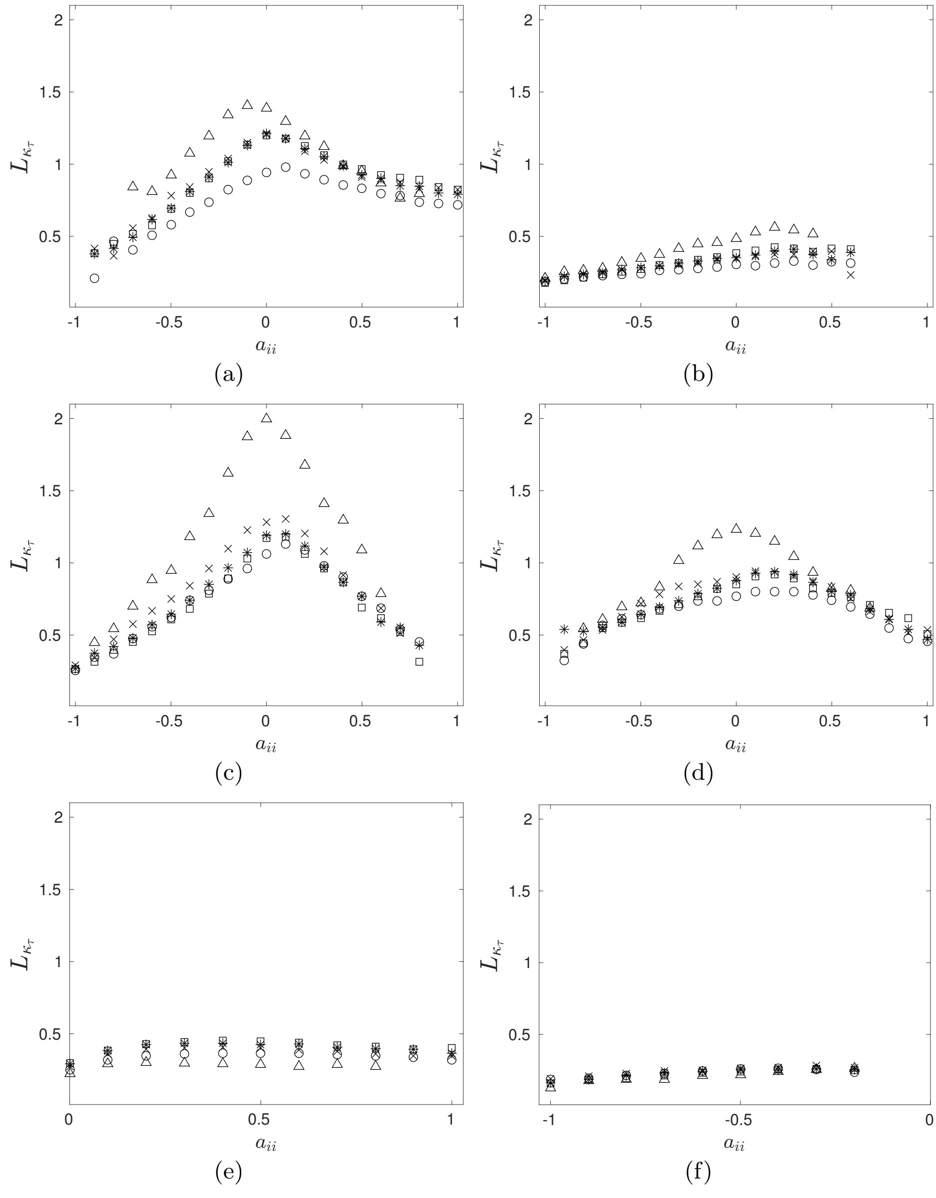

FIGURE 16. Variation of life of topology L_{κ_τ} with initial dilatation a_{ii} (bin size: $\overline{a_{ii}} \pm 0.05$) for 6 major topologies: (a)UNSS, (b)SNSS, (c)SFS, (d)UFC, (e)UFS and (f)SFC. Symbol $\triangle$, $\square$, $*$, $\times$, and O represents life-time of topology for simulations E, F, G, H and I respectively.

Life-times (L_κ) for SFS and UFC topology are shown in Figure 16(c) and 16(d) respectively. It can be seen that both SFS and UFC topologies exhibit monotonic rise, peaking in value for small positive dilatation, followed by monotonic fall while moving from negative dilatation to positive dilatation. The variation is approximately symmetric, slightly skewed towards positive values of dilatation. Variation ofL_κ with initial dilatation for UFS and SFC topology are shown in Figure 16(e) and 16(f) respectively. UFS and SFC topologies have smaller L_κ and shows small variation with dilatation in their respective regions of existence ($a_{ii} > 0$ for UFS and $a_{ii} < 0$ for SFC).

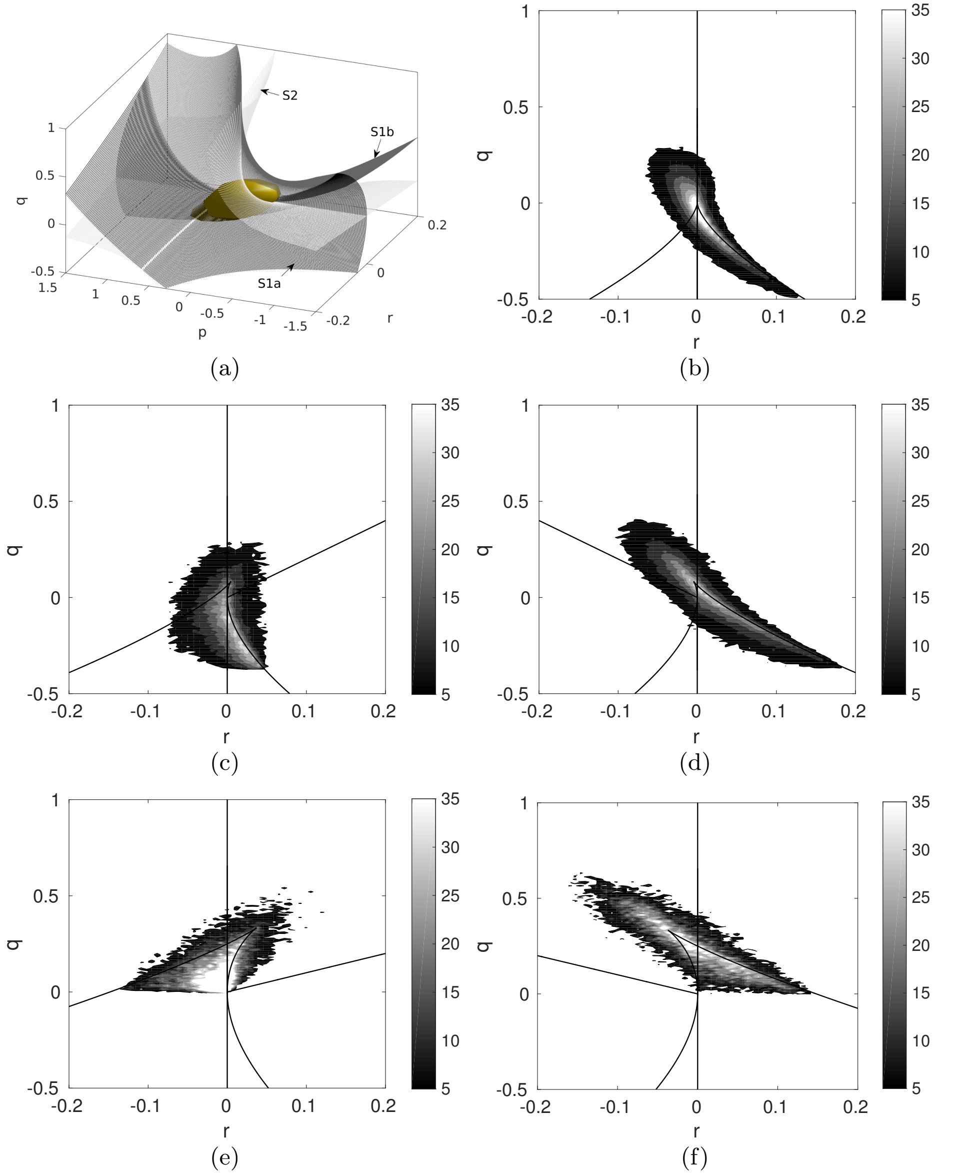

FIGURE 17. Population spread of particles in p-q-r space shown as (a) surface plot of region of high density (> 50% of maximum density) and Joint-PDF of population of particles at discrete planes of dilatation: (b)$a_{ii} = 0$, (c)$a_{ii} = -0.5$, (d)$a_{ii} = +0.5$, (e)$a_{ii} = -1$, (f)$a_{ii} = +1$

Hence, effect of initial dilatation is found to be maximum in UNSS and SFS topologies, followed by UFC topology, while other topologies, with low global life-times seem to exhibit mild variation in their life-times with varying initial dilatation.

7. Conclusions

We investigate the performance of the LLDM model of Jeong & Girimaji (2003) by comparing the evolution of the LLDM model term with the exact viscous term. Further, we compare the mean Lagrangian trajectory of fluid particles (MLT) with CMT and investigate the lifetime of different topologies using exact Lagrangian trajectories (ELTs). Well-resolved direct numerical simulations (up to 1024^3) of compressible decaying isotropic turbulence with Reynolds number up-to 350 and Mach number up-to 1.5 are employed to perform our studies. Along with this, a spline-interpolation based Lagrangian particle tracker is used to track an identified set of fluid particles (at t_{ref}) and extract their Lagrangian statistics.

We found that the time evolution of the exact viscous term $\left|\frac{\partial^2 A_{ij}}{\partial x_k \partial x_k}\right|$ shows a two-stage behavior. Its evolution is independent of turbulent Mach number. However, it's evolution is intensified at an elevated magnitude of dilatation. Further, we find that the exact viscous process occurs at an amplified rate for rotation dominated topologies as compared to strain-dominated topologies.

While comparing LLDM model term with the exact viscous term, we found that LLDM model grossly overestimates the exact viscous process. LLDM model term undergoes an exaggerated monotonic rise with time, failing to replicate the 2-stage evolution behaviour of the exact viscous term. We find that this anomaly in behaviour can be attributed to the LLDM modelling assumption of the isotropy of the inverse right Cauchy Green tensor C^{-1} and the $\frac{\partial^2 A_{ij}}{\partial X_m \partial X_n}$ tensor.

The actual motion of fluid particles in p-q-r space seems to show no particular tendency to move in clockwise spiral orbit around the origin, as indicated by instantaneous CMTs. In fact, there seems to be significant movement in the anticlockwise direction as well. A group of chosen fluid particles are found to move randomly such that in very short times (≈ 1 eddy-turnover time) the particles distribution mimics the global distribution, which remains almost constant for fully developed turbulent flow. Computations for mean life-time of topology reveals the following order of stability:

(i) Incompressible:

$$SFS \longrightarrow UFC \longrightarrow UNSS \longrightarrow SNSS$$

(ii) Mildly Compressible:

$$SFS \longrightarrow UNSS \longrightarrow UFC \longrightarrow SNSS \longrightarrow UFS \longrightarrow SFC \longrightarrow UNUNUN \longrightarrow SNSNSN.$$

(iii) Highly Compressible:

$$SFS \longrightarrow UNSS \longrightarrow UFC \longrightarrow UFS \longrightarrow SNSS \longrightarrow SFC \longrightarrow UNUNUN \longrightarrow SNSNSN.$$

The lifetime reduces with turbulent Mach number for topologies existing in the $p = 0$ plane (UNSS, SNSS, SFS, UFC). However, for topologies existing at high dilatation levels viz. UFS, SFC, SNSNSN and UNUNUN, the lifetime first increases and later show little variation with M_t. Reynolds number seems to have a negligible influence on the lifetime of topology. Further, the lifetime of topology is found to decrease with increasing magnitude of dilatation ($|a_{ii}|$).

The authors acknowledge the computational support provided by the High-Performance Computing (HPC) Center of the Indian Institute of Technology Delhi, New Delhi, India.

REFERENCES

Ashurst, Wm. T., Kerstein, A. R., Kerr, R. M. & Gibson, C. H. 1987 Alignment of vorticity and scalar gradient with strain rate in simulated Navier–Stokes turbulence. *Phys. Fluids* **30** (8), 2343–2353.

Atkinson, Callum, Chumakov, Sergei, Bermejo-Moreno, Ivan & Soria, Julio 2012

Lagrangian evolution of the invariants of the velocity gradient tensor in a turbulent boundary layer. *Phys. Fluids* **24** (10), 105104.

Bechlars, P. & Sandberg, R. D. 2017 Evolution of the velocity gradient tensor invariant dynamics in a turbulent boundary layer. *J. Fluid Mech.* **815**, 223242.

Bhatnagar, Akshay, Gupta, Anupam, Mitra, Dhrubaditya, Pandit, Rahul & Perlekar, Prasad 2016 How long do particles spend in vortical regions in turbulent flows? *Phys. Rev. E* **94** (5), 1–8.

Cantwell, Brian J. 1992 Exact solution of a restricted Euler equation for the velocity gradient tensor. *Phys. Fluids A* **4** (4), 782–793.

Cantwell, Brian J. 1993 On the behavior of velocity gradient tensor invariants in direct numerical simulations of turbulence. *Phys. Fluids A* **5** (8), 2008–2013.

Chen, Hudong, Herring, Jackson R., Kerr, Robert M. & Kraichnan, Robert H. 1989 Non-Gaussian statistics in isotropic turbulence. *Phys. Fluids A* **1** (11), 1844–1854.

Chertkov, Michael, Pumir, Alain & Shraiman, Boris I. 1999 Lagrangian tetrad dynamics and the phenomenology of turbulence. *Phys. Fluids* **11** (8), 2394–2410.

Chevillard, Laurent & Meneveau, Charles 2006 Lagrangian dynamics and statistical geometric structure of turbulence. *Phys. Rev. Lett.* **97** (17), 174501.

Chevillard, Laurent & Meneveau, Charles 2011 Lagrangian time correlations of vorticity alignments in isotropic turbulence: Observations and model predictions. *Phys. Fluids* **23** (10), 101704.

Chong, M. S., Perry, A. E. & Cantwell, B. J. 1990 A general classification of three-dimensional flow fields. *Phys. Fluids A* **2** (5), 765–777.

Chu, You-Biao & Lu, Xi-Yun 2013 Topological evolution in compressible turbulent boundary layers. *J. Fluid Mech.* **733**, 414–438.

Danish, Mohammad, Sinha, Sawan Suman & Srinivasan, Balaji 2016*a* Influence of compressibility on the lagrangian statistics of vorticity–strain-rate interactions. *Phys. Rev. E* **94** (1), 013101.

Danish, Mohammad, Suman, Sawan & Girimaji, Sharath S 2016*b* Influence of flow topology and dilatation on scalar mixing in compressible turbulence. *J. Fluid Mech.* **793**, 633–655.

Danish, Mohammad, Suman, Sawan & Srinivasan, Balaji 2014 A direct numerical simulation-based investigation and modeling of pressure Hessian effects on compressible velocity gradient dynamics. *Phys. Fluids* **26** (12), 126103.

Elghobashi, S. & Truesdell, G. C. 1992 Direct simulation of particle dispersion in a decaying isotropic turbulence. *J. Fluid Mech.* **242**, 655700.

Girimaji, S.S. 1991 Assumed β-pdf Model for Turbulent Mixing: Validation and Extension to Multiple Scalar Mixing. *Combustion Science and Technology* **78** (4-6), 177–196.

Girimaji, Sharath S. & Speziale, Charles G. 1995 A modified restricted Euler equation for turbulent flows with mean velocity gradients. *Phys. Fluids* **7** (6), 1438–1446.

Jeong, Eunhwan & Girimaji, Sharath S. 2003 Velocity-gradient dynamics in turbulence: Effect of viscosity and forcing. *Theor. Comp. Fluid Dyn.* **16** (6), 421–432.

Kerimo, Johannes & Girimaji, Sharath S. 2007 Boltzmann–BGK approach to simulating weakly compressible 3D turbulence: comparison between lattice Boltzmann and gas kinetic methods. *J. Turbul.* **8** (46), 1–16.

Kumar, G., Girimaji, Sharath S. & Kerimo, J. 2013 WENO-enhanced gas-kinetic scheme for direct simulations of compressible transition and turbulence. *J. Comput. Phys.* **234**, 499–523.

Lee, Sangsan, Lele, Sanjiva K. & Moin, Parviz 1991 Eddy shocklets in decaying compressible turbulence. *Phys. Fluids A* **3** (4), 657–664.

Liao, Wei, Peng, Yan & Luo, Li-Shi 2009 Gas-kinetic schemes for direct numerical simulations of compressible homogeneous turbulence. *Phys. Rev. E* **80** (4), 046702.

Lozano-Durán, Adrián, Holzner, Markus & Jiménez, Javier 2015 Numerically accurate computation of the conditional trajectories of the topological invariants in turbulent flows. *Journal of Computational Physics* **295**, 805–814.

Lüthi, Beat, Tsinober, Arkady & Kinzelbach, Wolfgang 2005 Lagrangian measurement of vorticity dynamics in turbulent flow. *J. Fluid Mech.* **528**, 87–118.

Martín, Jesús, Ooi, Andrew, Chong, M.S. & Soria, Julio 1998 Dynamics of the velocity gradient tensor invariants in isotropic turbulence. *Phys. Fluids* **10**, 2336–2346.

Martín, M Pino, Taylor, Ellen M, Wu, Minwei & Weirs, V Gregory 2006 A bandwidth-optimized WENO scheme for the effective direct numerical simulation of compressible turbulence. *J. Comput. Phys.* **220** (1), 270–289.

Meneveau, Charles 2011 Lagrangian dynamics and models of the velocity gradient tensor in turbulent flows. *Annu. Rev. Fluid Mech.* **43**, 219–245.

Ohkitani, Koji 1993 Eigenvalue problems in three-dimensional Euler flows. *Phys. Fluids A* **5** (10), 2570–2572.

O'Neill, Philippa & Soria, Julio 2005 The relationship between the topological structures in turbulent flow and the distribution of a passive scalar with an imposed mean gradient. *Fluid Dyn. Res.* **36** (3), 107–120.

Ooi, Andrew, Martin, Jesus, Soria, Julio & Chong, M.S. 1999 A study of the evolution and characteristics of the invariants of the velocity-gradient tensor in isotropic turbulence. *J. Fluid Mech.* **381**, 141–174.

Parashar, N., Sinha, S. S., Danish, M. & Srinivasan, B. 2017*a* Lagrangian investigations of vorticity dynamics in compressible turbulence. *Physics of Fluids* **29** (10), 105110.

Parashar, N., Sinha, S. S., Srinivasan, B. & Manish, A. 2017*b* Gpu-accelerated direct numerical simulations of decaying compressible turbulence employing a gkm-based solver. *Int. J. Numer. Meth. Fluids* **83** (10), 737–754.

Pirozzoli, S. & Grasso, F. 2004 Direct numerical simulations of isotropic compressible turbulence: influence of compressibility on dynamics and structures. *Phys. Fluids* **16** (12), 4386–4407.

Pope, Stephen B. 2002 Stochastic Lagrangian models of velocity in homogeneous turbulent shear flow. *Phys. Fluids* **14** (5), 1696–1702.

Pumir, Alain 1994 A numerical study of the mixing of a passive scalar in three dimensions in the presence of a mean gradient. *Phys. Fluids* **6** (6), 2118–2132.

Samtaney, Ravi, Pullin, Dale I. & Kosovic, Branko 2001 Direct numerical simulation of decaying compressible turbulence and shocklet statistics. *Phys. Fluids* **13** (5), 1415–1430.

Soria, J., Sondergaard, R., Cantwell, B. J., Chong, M. S. & Perry, A. E. 1994 A study of the fine-scale motions of incompressible time-developing mixing layers. *Phys. Fluids* **6** (2), 871–884.

Suman, S. & Girimaji, S. S. 2009 Homogenized Euler equation: a model for compressible velocity gradient dynamics. *J. Fluid Mech.* **620**, 177–194.

Suman, Sawan & Girimaji, Sharath S. 2010*a* On the invariance of compressible Navier–Stokes and energy equations subject to density-weighted filtering. *Flow Turbul. Combust.* **85** (3-4), 383–396.

Suman, Sawan & Girimaji, Sharath S. 2010*b* Velocity gradient invariants and local flow-field topology in compressible turbulence. *J. Turbul.* **11** (2), 1–24.

Suman, Sawan & Girimaji, Sharath S. 2012 Velocity-gradient dynamics in compressible turbulence: influence of Mach number and dilatation rate. *J. Turbul.* **13** (8), 1–23.

Vieillefosse, P. 1982 Local interaction between vorticity and shear in a perfect incompressible fluid. *J. Phys.* **43** (6), 837–842.

Xu, Haitao, Pumir, Alain & Bodenschatz, Eberhard 2011 The pirouette effect in turbulent flows. *Nature Phys.* **7** (9), 709–712.

Xu, K., KIM, CHONGAM, MARTINELLI, LUIGI & JAMESON, ANTONY 1996 BGK-based schemes for the simulation of compressible flow. *Int. J. Comput. Fluid D.* **7** (3), 213–235.

Yeung, P. K. & Pope, S. B. 1988 An algorithm for tracking fluid particles in numerical simulations of homogeneous turbulence. *J. Comput. Phys.* **79** (2), 373–416.

Yeung, P. K. & Pope, S. B. 1989 Lagrangian statistics from direct numerical simulations of isotropic turbulence. *J. Fluid Mech.* **207**, 531–586.